Engineering Fracture Mechanics 205 (2019) 57–69

Contents lists available at ScienceDirect

Engineering Fracture Mechanics

journal homepage: www.elsevier.com/locate/engfracmech

Fracture mechanics methods for evaluating the adhesion of cold spray deposits

B.C. White[a], William A. Story[b], L.N. Brewer[b], J.B. Jordon[a,*]

[a] The University of Alabama Dept. of Mechanical Engineering, Tuscaloosa, AL 35487, USA
[b] The University of Alabama Dept. of Metallurgical and Materials Engineering, Tuscaloosa, AL 35487, USA

ARTICLE INFO

Keywords:
Cold spray
Fracture
Adhesion
Aluminum

ABSTRACT

The adhesion strength of cold sprayed (CS) AA7075 deposits made with varying surface preparations was measured using two fracture toughness methods, and compared to the more common ASTM C633 adhesion test. The ASTM C633 test was found to be limited by the cohesive strength of the deposit, or most commonly the bond strength of the epoxy used (~75 MPa). Using a unique interfacial compact tension (CT) specimen, $K_{I,eff}$ values were found to range between 1.25 and 1.90 MPa √m with a linear relationship between the substrate roughness and the interface toughness. A mixed mode I/II four-point bend test found significantly higher interface toughness values of around 4.87 MPa √m, and no clear dependence on surface roughness. Residual stresses were found to cause problems with cracking in the interface CT specimens, and more generally to change the measured adhesion values for all test methods. The deformation of the four-point bend specimens caused by residual stresses allowed for a direct measurement of the effects of residual stresses on the interfacial toughness, which was found to be 35% of the measured value.

1. Introduction

Additive repair has the potential to allow the repair or rebuilding of large or expensive parts at minimal cost. One process that is particularly adaptable to additive repair is cold gas dynamic spraying (CS). Cold spray uses high pressure gas to accelerate powder particles to velocities ranging from 300 to 1500 m/s [1]. The powder particles impact the substrate with enough kinetic energy to severely plastically deform and metallurgically bond to the substrate. The CS method is an ideal technology for additive repairs because low temperatures are maintained throughout the process so that the substrate, often a load carrying structural member, will not be thermally damaged [1,2]. This minimal thermal input is especially critical when repairing aluminum components common in the aerospace industry, which experience a decline in strength after exposure to temperatures as low as 140 °C [3].

While similar to additive manufacturing, additive repair is set apart by the fact that the repair will contain a substrate (the part to be repaired), and a deposit of new material, and thus an interface. This interface can be the weakest link in the repair, and clearly poor adhesion will lead to a poor repair. In fact, a repair that completely de-bonds can be more detrimental than no repair at all, as it may separate and cause foreign object damage (FOD). FOD is a serious maintenance issue for inspection crews in both civilian and military aviation operations. A report from the Naval Safety Center detailing the prevalence and type of FOD over five years from 2004 to 2009 shows 30 non-bird FOD mishaps, with 10 percent of these mishaps resulting in damage to the aircraft engines caused by fasteners [4]. Since one specific application of CS is to repair corrosion damage that occurs around fasteners on aircraft, assessing and

* Corresponding author.
E-mail address: bjordon@eng.ua.edu (J.B. Jordon).

https://doi.org/10.1016/j.engfracmech.2018.11.009
Received 13 August 2018; Received in revised form 2 November 2018; Accepted 3 November 2018
Available online 03 November 2018
0013-7944/

Nomenclature

a	crack length
B	width of four point bend specimen
E	elastic modulus
$\bar{E}$	plane strain elastic modulus
F	geometry factor for stress intensity solution
G	energy release rate
G_C	critical energy release rate
G_{eff}	effective (measured) energy release rate
H	thickness of composite four point bend specimen
H_1	thickness of deposit portion of four point bend specimen
H_2	thickness of substrate portion of four point bend specimen
I	second moment of area
K	stress intensity factor
K_{Ic}	critical mode one fracture toughness
$K_{I,eff}$	effective (measured) mode one fracture toughness
$K_{I,G.B.}$	average mode I fracture toughness of the grit blasted samples
K_Q	conditional fracture toughness measurement
$K_{I,\ Sand}$	average mode I fracture toughness of the sanded samples
L	distance between inner and outer loading pins in the four point bend test
M	moment endured by four point bend specimens
M_{app}	moment applied to four point bend specimen
M_{RS}	moment in four point bend specimen due to residual stress
S22	normal stress in the 2 (y) direction
ρ	radius of curvature of four point bend specimen
σ	nominal stress
σ_{Sand}	average failure stress of the sanded ASTM C633 samples
$\sigma_{G.B.}$	average failure stress of the grit blasted ASTM C633 samples
CS	cold spray
CT	compact tension (specimen)
FEA	finite element analysis

optimizing the adhesion strength of these repairs is critical.

The adhesion strength of CS repairs is attributed to both metallurgical bonding and mechanical interlocking, both of which may depend on the surface roughness of the substrate. In particular, Samson et al., studying AA6061-AA6061 systems [5], and Kumar studying pure Al on steel and Cu-Cu systems [6], found adhesion strength to generally increase with increasing surface roughness up to a certain critical roughness, then decrease again at very high roughnesses. Interestingly, however, Samson et al. and Perton studying Ti-6Al-4V on Ti-6Al-4V [7], found adhesion strength to increase again on mirror polished surfaces. These complicated relationships may result from competition between mechanical interlocking and metallurgical bonding which each have their own dependence on substrate surface roughness. One possible explanation for this behavior is that very smooth mirror polished surfaces enhance metallurgical bonding, while the addition of small micro roughness merely provides obstacles to metallurgical bonding without adding any appreciable mechanical interlocking. Rougher surfaces however may offset this effect by providing a significant mechanical interlocking component.

Currently the adhesion of CS deposits is most commonly tested in accordance with ASTM C633 by gluing a threaded bar to the repair and pulling normal to the interface until the glue or the deposit fails [1]. Adhesion values for CS AA7075 sprayed with helium measured by this method range from 30 to over 84 MPa [1,8]. While this test offers a pass/ fail criterion that is likely sufficient, it does not allow any detailed analysis and suffers from a number of serious drawbacks. Most notably the test can only measure adhesion strengths up to the strength of the epoxy (~75 MPa), and most high strength epoxies must be heat cured, including the most commonly used FM-1000 (Cytec Industries), which requires curing at temperatures of 175 °C for an hour. These temperatures are enough to slightly lower the strength of AA7075, but more importantly they can relax residual stresses significantly (up to 36%). Both of these effects are quantified by Younger and Eckelmeyer [9]. This is important because residual stresses play a large role in the adhesion of the deposit, and in fact thick CS deposits can sometimes delaminate without any applied stress. Several sources have shown that residual stress, which is strongly dependent on deposit and layer thickness, has a considerable effect on the ASTM C633 adhesion strength [10,11]. Furthermore thin coatings are by definition in a state of plane stress, and so should never experience the type of normal tensile loading that is measured using ASTM C633. A more rigorous alternative adhesion test method that does not rely on glue is the lug shear test (MIL-J-24445A), which has recently become more popular for testing CS coatings [8,12,14]. Fundamentally however, a fracture toughness parameter is needed because the CS bulk material, and especially the interface, is very brittle and contains flaws.

There exist several fracture-based methods for measuring adhesion such as interface indention [1,15], and a variety of peel type tests and K_{Ic} geometries [16,17] that have potential to be applied to CS coatings. The present work examines two fracture based adhesion tests, an interfacial compact tension (CT) K_{Ic}, and an interfacial four-point bend test. While these test methods have been used on a variety of bulk materials and interfaces, to the best of the authors' knowledge there exists no published work on the fracture toughness of cold spray interfaces of any material system. The fracture toughness of bulk CS deposits however has received some limited attention [18–20], though in many ways the toughness of the interface is a more critical parameter because it is generally lower than that of the bulk material and directly controls the adhesion of the repair. Fracture mechanics parameters for adhesion will give a much more thorough understanding of the microstructure-property relationships, and most importantly will allow for flaw tolerant design.

2. Materials and methods

2.1. Cold spray processing

The thicker substrates used in the interfacial CT and ASTM C633 adhesion tests were AA7075-T651, while the thinner substrates used for the four-point bend test were AA7075-T6. All substrates for each test method were prepared for spraying in the same manner using three different surface roughening techniques: grit blasting using 60 grit garnet at 620 kPa (90 psi), non-directional (random orbit) hand sanding with 60 grit SiC sandpaper, and milling. The milling direction was made parallel to the long raster direction of the CS and parallel to the crack growth direction in the interfacial CT specimens. After roughening, the samples were de-greased with detergent and rinsed with isopropanol immediately prior to spraying. The surface roughness that resulted from the three surface preparation techniques was measured using a 2 mm linear scan parallel to the raster/crack growth direction in three separate locations on each surface, using a Dektak IIA surface profilometer.

The CS deposits were made with a VRC Gen III high pressure CS system. Dried, but otherwise un-modified commercially available, gas atomized AA7075 -325 mesh powder produced by Valimet Inc. was used as the feedstock powder with commercially pure helium as the carrier gas. The deposits were made using the deposition parameters listed in Table 1, where the temperature was measured at the top of the nozzle. A polybenzimidazole nozzle with a 2.0 mm throat diameter, a 4.5 mm exit diameter, and total length of 120 mm was used. The deposition parameters were held constant between all three test geometries, however the four-point bend samples necessitated thinner machined deposits. The thickness of all deposits was machined down to provide a flat surface, and to remove the last layer of material which may not have bonded properly.

2.2. ASTM C633 adhesion test

The specimens for this test were manufactured by spraying a 2.5 mm thick CS deposit on to a 31.75 mm diameter substrate. The diameter was then turned down to 25.4 mm to eliminate edge effects, and the surfaced machined flat. Since the sample is circular the raster direction does not matter. The CS surface was then bonded to another threaded slug using FM-1000 (Cytec Industries), and cured under a ~3.5 lbs clamping force at 175 °C for an hour. After fully curing, the samples were tested in displacement control at 1 mm/min.

2.3. Interfacial compact tension K_{Ic}

This test method proceeds in accordance to ASTM E399, with the exception that no fatigue pre-cracking was conducted. Fatigue pre-cracking could not be reliably carried out because of the brittle nature of the CS interface. The artificial starter notch also could not be machined traditionally, because the CS deposit is so thin that any notch would remove a large fraction of the deposit, reducing its strength and stiffness, and changing the residual stress state. Instead a sharp artificial notch was embedded at the interface during the CS deposition. After surface roughening the 25.4 mm thick substrate, a 0.4 mm thick aluminum sheet was glued with cyanoacrylate to the substrate in the area that would normally be machined into a notch. The edge of the shielding plate was then carefully ground to a chisel edge to produce the sharpest notch possible. The entire surface of the sample, including both the shielded and unshielded portions of the sample, was then sprayed over to produce a 2.5 mm thick CS deposit. The long raster direction was made parallel to the crack growth direction, as indicated in Fig. 1a. The CS deposit adhered to both the bare substrate, and the shielding plate, but did not bond with the portion of the substrate that was protected by the shielding plate. The CS surface was then ground flat, and the cyanoacrylate dissolved in acetone, leaving a sharp notch. Next, an aluminum block was attached to the CS surface using a structural epoxy. Finally, the holes were drilled in the substrate and top plate, and 6 mm thick, full sized compact tension specimens were cut from the composite block as shown in Fig. 1a. While this specimen does require gluing, the large notch at the CS interface means that the epoxy is relatively unstressed, so epoxy failure is unlikely. The composite CT sample was then loaded in displacement control at 1 mm/minute using a servo-hydraulic load frame with a 2.5 kN load cell.

2.4. Interface four-point bend

The interfacial four-point bend test, the test specimen for which is shown in Fig. 2, was established by Charalambides et al. [21,22]. This test was originally developed for measuring the adhesion of thin films, frequently for micro-electronics applications, though it has also been applied to plasma sprayed thermal barrier coatings that more closely resemble CS deposits [16,23,24]. The

Table 1
Cold Spray deposition parameters and deposit/substrate dimensions.

Test geometry	Pressure (MPa)	Temperature (°C)	Gun travel speed (mm/s)	Number of layers	Substrate thickness (mm)	Deposit thickness (mm)	Machined thickness (mm)
ASTM C633	2.9	415	200	4	38.1	2.5	1.91
Interfacial CT	2.9	415	200	4	25.4	2.5	1.95
Four-point bend	2.9	415	200	4	1.02	2.5	1.02

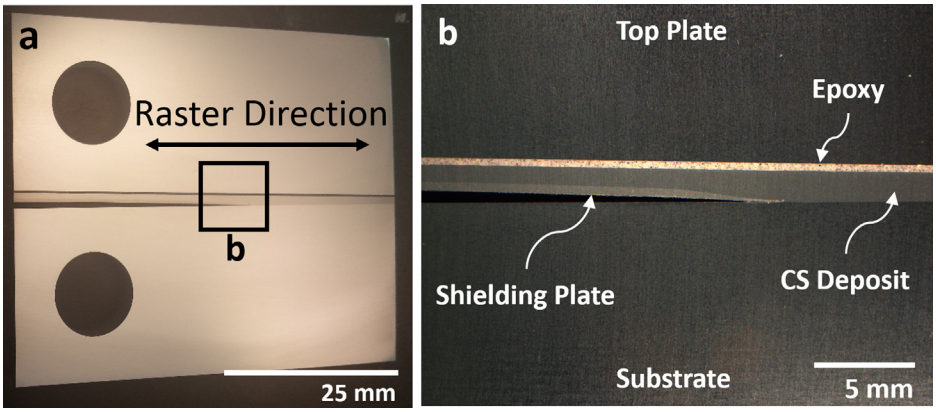

Fig. 1. Interface compact tension sample, showing the artificial notch created by the shielding plate.

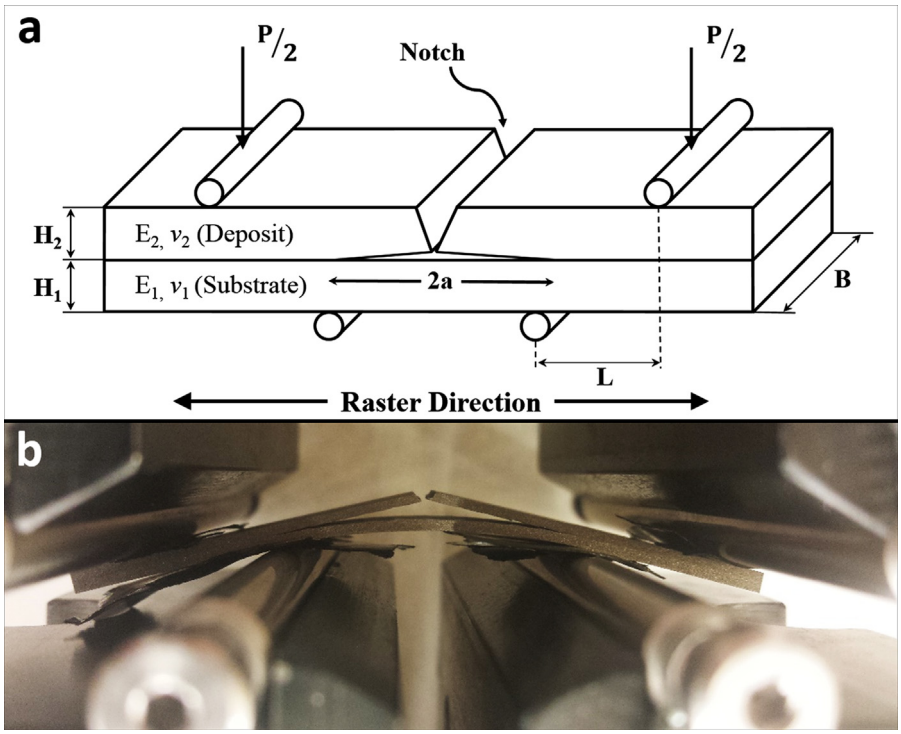

Fig. 2. Notched interfacial four-point bend specimen geometry.

mechanics of this test are outlined elsewhere [21,22,25], however it can be briefly summarized by realizing that the energy stored by bending the beam is released by the crack growing along the interface. At steady state, this produces an equilibrium where a constant load is required to grow the crack. The energy release rate for the symmetric system that is used in this paper is given by Eq. (1), where H is the total beam thickness, B the width of the beam, M is the applied moment, $\bar{E}$ the plane strain modulus, and I is the second moment of inertia for the composite beam.

$$G_c = \frac{21}{2}\frac{M^2}{3\bar{E}IB} = \frac{21}{2}\frac{L^2P^2}{\bar{E}B^2H^3} \tag{1}$$

While this test is mixed mode in nature the measured energy release rate gives only the energy released by the growing crack and not its mode I and mode II components or stress intensities. The modality however (usually expressed in terms of phase angle) can be determined numerically as by Charalambides et al., and can be varied from ~40 to 50° by changing the thickness or elastic modulus of the top and bottom portions of the beam. For the symmetric system used in this paper, the modality is around 42°, which is nearly 50% mode I and 50% mode II.

The specimens for this sample were made by simply spraying CS deposits on top of the roughened sheets with the long raster direction parallel to the length of the beam. The rectangular beams were then machined by wire EDM to the dimensions

$H_1 = H_2 = 1.016$ mm, B = 9.53 mm, and L = 12.7 mm. A notch was cut using EDM into CS deposit at the center of the beam, approximately 90% through the deposit. Since this test requires quasi-static crack growth, these dimensions were chosen to maximize the stability of the growing crack [25]. Because this test required such a thin substrate it was not possible to produce a milled surface without creating unacceptable distortion in the substrate.

The four-point bend test was carried out on a servo-hydraulic load frame with a 2.5 kN load cell. In order to achieve quasi static crack growth, a displacement rate of 0.1 μm/s was used. Because the displacement rate is so low, considerable efforts were made to dampen vibrations from the hydraulic systems. This was accomplished satisfactorily by lowering the dither amplitude responsible for oscillating the valves in the test frame, and turning the hydraulic pump pressure down to 2 MPa from 20 MPa, the latter of which was found to have the greatest effect. At the low pump pressure the variations in the displacement signal were found to be the same amplitude as when the pump is turned off completely, indicating that they result either from unavoidable facility vibrations, or more likely electronic noise. Graphite paper was placed between the loading pins and the sample to reduce friction. The four-point bend fixture was aligned with a strain-gauged beam, but because of the distortion in the CS samples, perfect alignment for each sample could not be guaranteed.

In order to estimate the effect of the residual stress on the interface toughness of the four-point bend specimens, the curvature of the beams, which can be seen in Fig. 3, was measured and related to the energy stored in the beam. This was done by imaging each specimen with vertical and horizontal reference dimensions. Then using a digitizing software, the exact positions of 15 points along the edge of the beam on both sides of the notch were recorded. With the edge of the beam converted to x-y coordinates, a circle was then fit to the data on each side of the notch. The curvatures from both sides were then averaged together and used to calculate an overall estimate for the residual stress energy stored in each beam.

3. Results

3.1. Interface characterization

The roughness profiles created by the three surface preparations are shown in Fig. 4. The grit blasted and sanded surfaces are non-directional, and their surface profile's seeming randomness reflects this. The milled surface profile however shows some periodicity from the tooling marks created with each rotation of the end mill. The milled surface roughness appears to have a much lower frequency than the other profiles, with relatively smooth transitions between peak and valley. The milled surface is roughest on a macro scale, which may allow for good mechanical interlocking, but on a micro scale (in-between peak and valley) it is actually quite smooth, which may enhance the ability of impacting particles to metallurgically bond. Any further analysis of this nature however must address the fractal nature of surface roughness which can quickly become quite burdensome. The surface profile, crack growth direction, long raster direction, and milling direction are parallel to each other.

The surface roughness produced by the three surface preparations are shown in Table 2. Despite using nominally the same sized media, grit blasting was found to produces a slightly smoother surface than hand sanding, while milling resulted in the roughest surface.

Images of the interface cross sections after cold spraying for all three surface preparations are shown in Fig. 5. The metallography samples were sectioned along the plane perpendicular to the interface and containing the crack growth direction. Good interface bonding was observed in all conditions, with occasional particles showing some lack of bonding as shown with an arrow in Fig. 5a. All three conditions show a scalloped interface, where the substrate has plastically deformed around the impacting particles. This deformation appears to dominate the original surface roughness, though in the case of the milled surface in particular, the impact deformation roughness may superimpose on top of the original roughness. The peak-to-trough distances for the scalloped interfaces, shown in Fig. 5, range from 3 μm to 10 μm, which is quite high when compared to the original substrate roughness profiles shown in Fig. 4.

3.2. Astm C633

Fig. 6 shows the normal tensile pull results from the ASTM C633 adhesion test. Fig. 6a shows the ASTM C633 results for the three surface preparations of interest to this study, as well as three additional conditions (finish milled, angle ground, and sanded with a CS deposit that is twice the thickness of the other deposits). Fig. 6b shows the grit blasted, sanded, and milled surface preparations used throughout this study plotted as a function of surface roughness. This test was conducted to provide a commonly used benchmark to which the fracture based tests can be compared. From Fig. 6a it is clear that epoxy failure is the most common type of failure, and

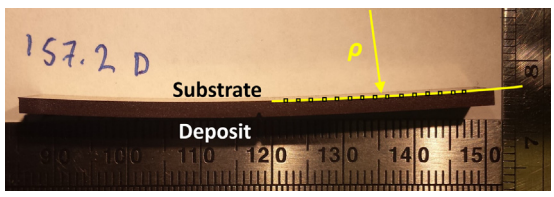

Fig. 3. Measurement of distortion caused by residual stresses.

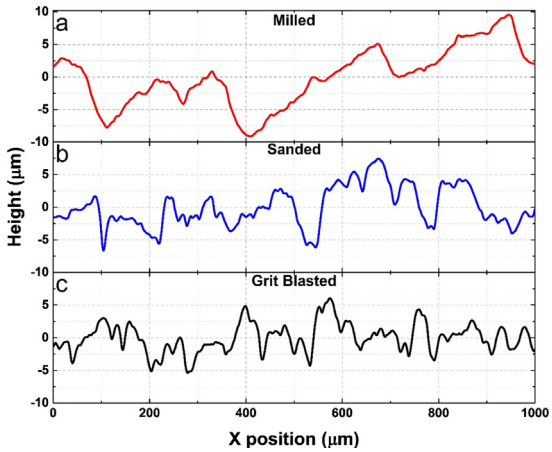

Fig. 4. Surface profiles of the substrates before cold spraying: (a) milled, (b) sanded and (c) grit blasted.

Table 2
Surface roughness produced by sanding, grit blasting and milling.

Surface condition	Surface roughness, Ra, (µm)
Grit blasted	2.17
Sanded	3.21
Milled	4.79

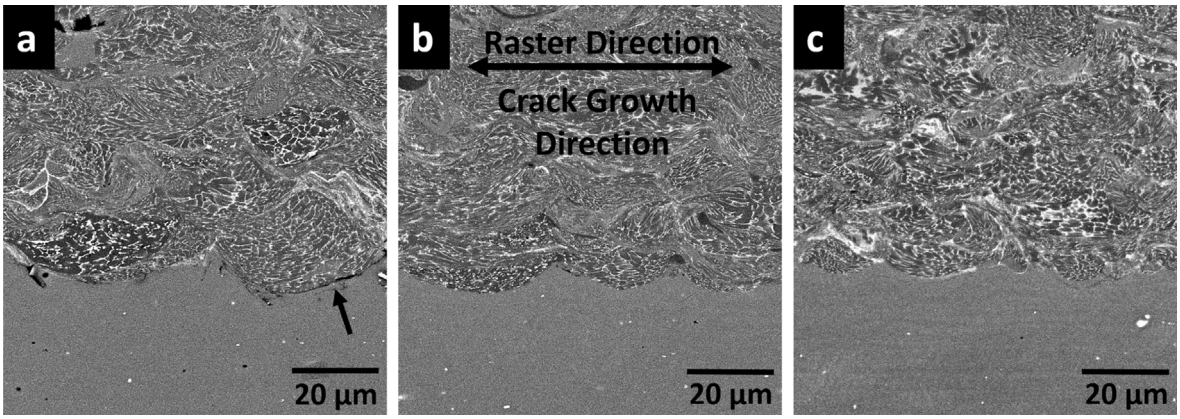

Fig. 5. Cross section of interface for each surface preparation method (a) grit blasted, (b) sanded, (c) milled.

while this is the preferred failure mode, it does nothing to help determine which surface preparation produces the best adhesion strength, and cannot differentiate between five of the six considerably different surface preparations. The exact cause for the cohesive failure found in the sanded samples is unknown, however the tensile strength of CS deposits in this direction is relatively low due to defects trapped in-between layers [26,27]. This provides another limitation to the ASTM C633 test that would still remain even if stronger epoxies could be used. It is interesting to note that the three conditions show essentially the same average strength for all conditions, but different failure modes. This makes it difficult to draw firm conclusions, however it is still possible to conclude that the milled surface, having no adhesion failures, is likely the strongest of the three, while the grit blasted surface, being the only condition to suffer multiple adhesive failures, likely has the lowest adhesion strength.

3.3. Interfacial compact tension K_{Ic}

Fig. 7 shows the results from the interfacial CT tests plotted as a function of substrate roughness. These results show a clear linear relationship between adhesion toughness and the surface finish, with the higher roughness surfaces having higher adhesion toughness. While these fracture toughness values appear to be relatively low, it is important to note that the bulk CS materials themselves are generally brittle and have low fracture toughness on the order of 3 MPa √m [18]. Because the measured K_Q values are low, the 6 mm thick samples easily surpass the ASTM E399 criteria for sample dimensions. However, the fracture toughness values

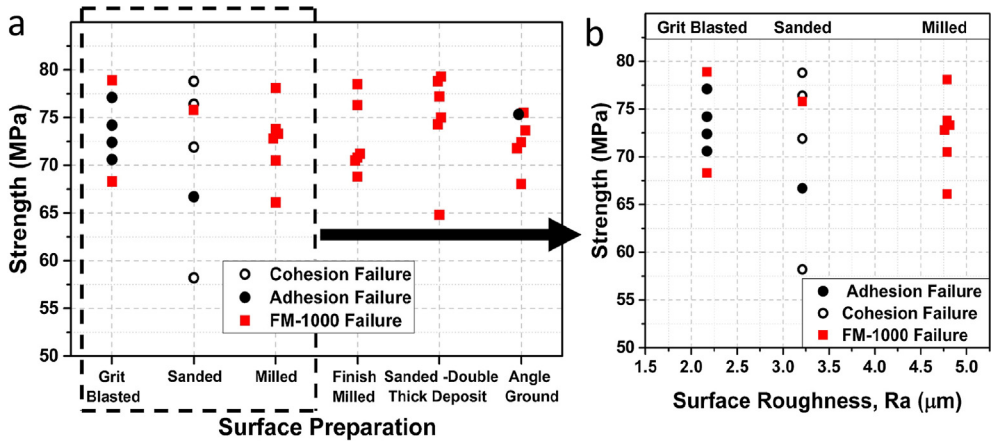

Fig. 6. (a) ASTM C633 Adhesion results for various surface preparations. (b) ASTM C633 adhesion results for the three surface preparations of interest to this study plotted as a function of surface roughness.

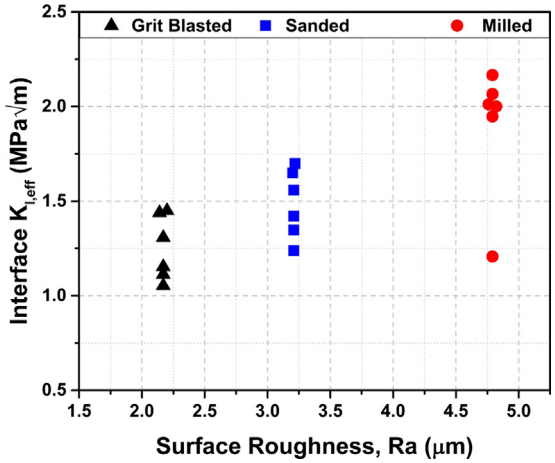

Fig. 7. Interfacial CT results for various surface preparations, plotted as a function of surface roughness.

obtained from this test are still considered to be an effective K_I (hereafter $K_{I,eff}$), rather than a K_{Ic} because these values encompass not only the interface property, but the considerable influences from residual stress. In fact, from Fig. 1, it can be seen that the notch was pulled open by the residual stresses, which would result in a lower measured $K_{I,eff}$. While the geometry dependence of residual

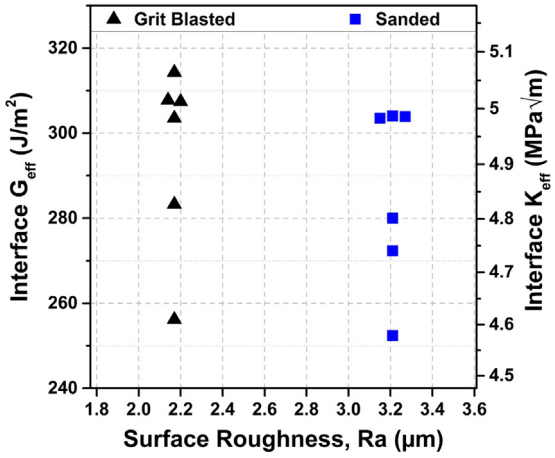

Fig. 8. Interfacial effective energy release rate for sanded and grit blasted surface preparations from notched four point bend test.

stresses prevent direct comparisons between different adhesion test methods, the residual stresses for the interfacial CT geometry should be the same from sample to sample, allowing for direct comparisons between surface preparation techniques. Note the low point from the milled condition is statistically an outlier ($p < 0.01$), however because no physical basis for this anomaly could be found, it is included in all data sets and analysis.

3.4. Interface four-point bend

Fig. 8 shows the critical energy release rate and a conversion to fracture toughness for the sanded and grit blasted surface preparations. The interfacial four-point bend test measures the energy release rate of the growing crack, G_{eff}, which for the plane strain conditions assumed in this test, can be converted to a fracture toughness value by the relation:

$$K = \sqrt{G \cdot \bar{E}} \tag{2}$$

The measured energy release rate is a combination of the mode I and mode II components, and is referred to simply as a mixed mode G, without attempting to separate the mode I and mode II contributions. As with the interfacial CT tests, an effective energy release rate is used so as to distinguish the measured result which includes residual stress effects from the interface property G_c. The residual stresses in this geometry act in the opposite direction from those in the CT K_{Ic} specimen, which increases the observed energy release rate.

While unfortunately the distortion that occurs from the milling surface preparation does not allow it to be compared here, the sanded and grit blasted preparations can be said to have nearly the same mixed mode adhesion toughness, as measured by this test. The similar mixed mode toughness values may mean that the adhesion toughness has little relationship with surface roughness, or this test is failing to capture this relationship with any appreciable sensitivity. It is possible that high residual stresses may be effectively hiding up the effects of the surface roughness. The mixed mode fracture toughness values appear to be quite high when compared to the mode I values obtained by the interfacial CT specimens. Mode II fracture toughness however is consistently reported as significantly higher than the mode I toughness, though there is disagreement on the magnitude of the difference, with sources for wrought AA7075 reporting values of 1.5 [28], 2.5 [29] and 4 [30] times higher than the mode I fracture toughness. In the present case, the crack path is prescribed by the interface, and the roughness of the interface may provide more interference to mode II opening than in mode I, possibly further increasing the difference between them.

3.5. Fractography

Fig. 9 shows representative plane view images of the substrates before cold spray deposition, and after the interfacial CT and four

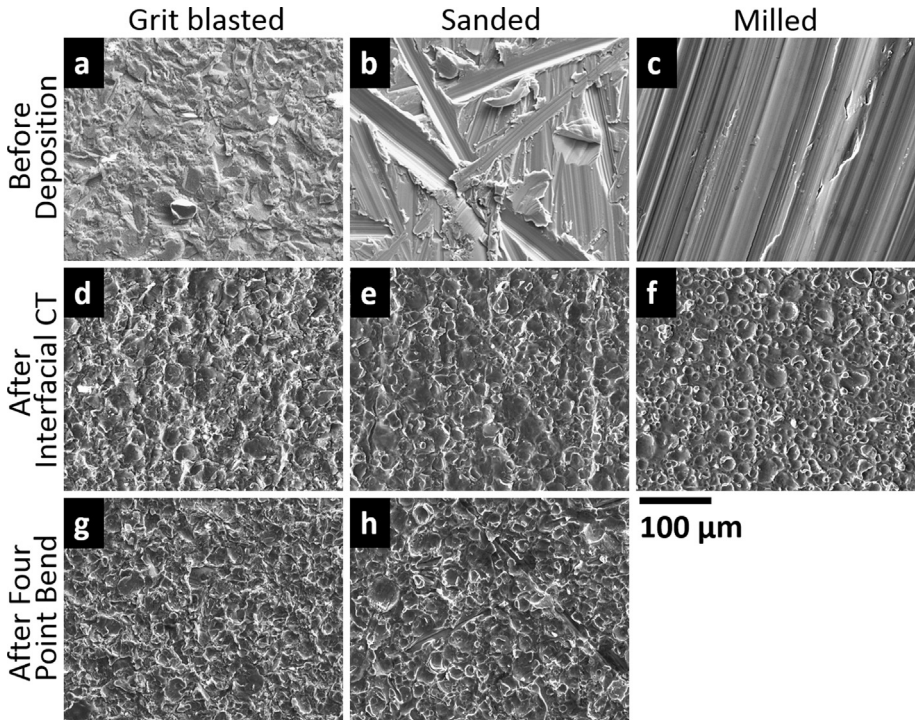

Fig. 9. Plane view images of the substrate prior to spraying, and the substrate side of the fracture surface after interfacial K_{IC} and four point bend tests.

point bend tests, for all three surface preparations. The images of the substrate side of the fracture surface were taken approximately at the center of the interfacial CT specimen, and midway between the inner loading pins and the center notch on the four point bend specimens. The images of the roughened substrates (Fig. 9a–c) show potential flaws such as burs left over from sanding and milling. Milling in particular has the potential to produce large burs that could act as critical flaws, so it is essential to de-bur any substrate that is to be sprayed over, especially along edges and interfaces between milling passes. Fig. 9h shows a rather deep valley that appears not to have been filled in by CS powder. If the valley is deep and narrow enough, powder particles may not be able to penetrate into the valley, or deform the peaks enough to reach the bottom of the valley, resulting in an embedded flaw. It should also be noted that these rough surface features may also initiate fatigue cracks perpendicular to the interface, especially if they are not filled in with properly bonded CS deposit.

Both the interfacial CT and four point bend fracture surfaces appear very similar, with all the substrates showing cratering from impacting powder particles, though these features are most clearly seen in Fig. 9f. The milled surface likely shows these features more clearly because it had a smoother original surface on this length scale. This substrate impact deformation at this length scale largely obscures the original substrate features, as was seen in the metallography cross sections. At larger length scales however, the macro features from sanding and milling are more recognizable. The prevalence of these craters show that the crack has grown almost entirely along the interface, underneath the first layer of CS particles; however in some places powder particles are still found adhered to the substrate.

4. Discussion

4.1. Residual stress effects

Residual stresses occur during CS as a result of the plastic deformation of the substrate and the impacting particles. These internal stresses can sometimes be high enough to delaminate thick deposits, without any externally applied stress, and will always affect the measured adhesion properties regardless of the test method. The mechanisms that cause residual stresses in *thin* CS coatings can be easily understood as being the same as those that occur during shot peening [1], and generally produces stress profiles of similar shape, with peak stresses in the range of 100 to −200 MPa [10,11,13]. A more detailed discussion is given by Cavaliere and Silvello who explain the dependence of residual stresses on the CS processing conditions for AA2024 and AA7075 [13]. While residual stresses are dramatically affected by the processing conditions (namely particle velocity and temperature) they are also highly geometry dependent, particularly on the layer, total deposit, and substrate thicknesses of the system, which have been shown to affect the adhesion strength of the deposits [10–12]. Furthermore post spray sample preparation such as cutting into test specimens, or heat curing of epoxy may alter or relax the original residual stresses. Because of this geometry dependence, the effects of residual stress are difficult to account for and may not be the same across different components, or adhesion testing geometries. In particular both the CS deposit and substrate in the four-point bend specimens are significantly thinner than in the other test geometries. The deformation that occurs in the thin substrates used in the interfacial four-point bend test however gives a convenient method for estimating the effects of residual stresses on the adhesion toughness. Because of the stress concentrating notch used in the interfacial CT specimens,

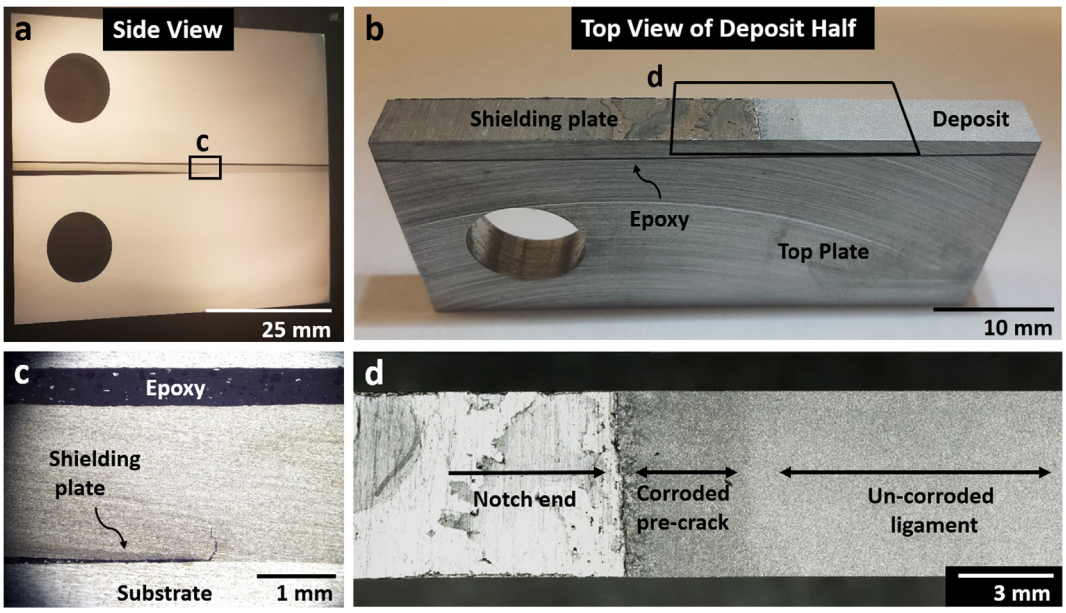

Fig. 10. Example of branched and pre-cracks in interfacial CT samples: (a) side view of an interfacial CT sample, (b) top view of deposit half of a fractured interfacial CT sample, (c) higher magnification image of the branched crack, (d) annotated close up image showing the pre-crack.

this geometry is susceptible to cracking, both along the interface as previously shown, and to branched cracks emanating from the notch tip.

All of the interfacial CT samples were found to be pre-cracked by residual stresses before testing, an example of which is shown in Fig. 10b and d. The extent of the pre-crack can be seen by corrosion from cutting fluid, or dissolved cyanoacrylate residue on the fracture surface resulting from sample preparation. Most pre-cracks were found to be within 1–4 mm with the smallest observed pre-crack being 0.5 mm. The pre-crack length in this case was not found to correlate with the measured interfacial fracture toughness, and is likely a result of sample preparation combined with the effects of residual stress. While the residual stresses may alter the measured fracture toughness, the pre-cracking should act in much the same way as fatigue pre-cracking, increasing the sharpness of the notch and providing a more accurate representation of realistic crack tip conditions. The pre-crack crack length (defined as the average of the lengths measured from both sides of the sample) was treated exactly as if it were a fatigue pre-crack, and was included in the crack length when calculating the $K_{I,eff}$ values.

Of particular concern to the validity of the interfacial CT tests are the branched cracks emanating from the notch tip which were found on many of the samples (Fig. 10c). These cracks are attributed to residual stresses from the CS process, which caused the deposit to bend upwards and crack at the stress concentration caused by the notch. The largest branched crack found, shown in Fig. 10c, was approximately 430 μm long. Branched crack problems have been studied extensively, with Thoecaris offering solutions for asymmetrical branched cracks that closely resemble the crack geometry in Fig. 10c [31,32]. As the ratio of the lengths of the branched cracks, or the angle between the branched crack increases, the effect of the shorter branch on the longer branch is diminished. The 90°-0° orientation of the cracks in the interfacial CT samples should show even less of an interaction, than the geometries used by Theocaris, however this should be confirmed using finite element analysis (FEA).

To examine the effect of the branched crack on the K_{Ic} solution for the CT specimens, a 2d linear-elastic, plane strain, finite element model was employed. To increase the fidelity of the model a 0.3 mm thick layer of epoxy with a modulus of 3 GPa was included. Both 0.3 and 0.5 mm branched cracks were used in the model at various distances behind the main crack tip. Mesh refinement convergence, while not shown, was found to occur by 0.05 mm, however the computational costs for the 2d elastic model are so low that a 0.01 mm mesh was used in a 1 mm radius circle around the crack tips. The CT specimen model where the 0.5 mm branched crack is 0.5 mm behind the main crack tip, is shown in Fig. 11. In Fig. 11b it can be seen that the opening (S22) stress contours around the main crack show very little interaction with the branched crack.

The finite element results, presented in Fig. 12, show that as the distance between the branched crack and the main crack tip increases, the stress intensity at the main crack converges to that of the case with no branched crack. This convergence occurs approximately when the main crack extends ahead of the branched crack, a distance farther than the length of the branched crack, as suggested by Theocaris [31,32]. The limited effect of the branched crack can be explained by the loading condition, which is perpendicular to the main crack and parallel to the direction of the branched crack. The largest branched crack found in the experimental samples was 0.43 mm, while all the pre-crack lengths were found to be greater than 0.5 mm, with most being 1–4 mm in length. Thus, we are confident that in this case the branched cracks are not significantly affecting the measured $K_{I,eff}$. However, this may not be true for a CS deposit with a higher adhesion toughness, which should reduce the pre-crack length, or a lower cohesion toughness, which should increase the branched crack length, or for geometries with higher residual stresses. Also shown in Fig. 12, is a 4.7% difference between the finite element and analytical (ASTM E399) solutions. This discrepancy is caused by the low modulus of the epoxy used in the finite element model that is not represented in the analytical solution. Because the difference is relatively small, the analytical solution was used for all fracture toughness calculations to maintain consistency.

The residual stresses in the four-point bend sample visibly deformed the rectangular beams, as shown in Fig. 3. This bending is directly proportional to the stored energy, and can be quantified by measuring the radius of curvature of the beam. Since the interfacial four-point bend test measures the energy that is released as the crack grows, the energy stored by the residual stresses is easily subtracted from the energy stored by the applied moment. Alternatively, the radius of curvature can be used to find the moment that is caused by the residual stresses, which can then be subtracted from the applied moment as shown in Eq. (3). In this

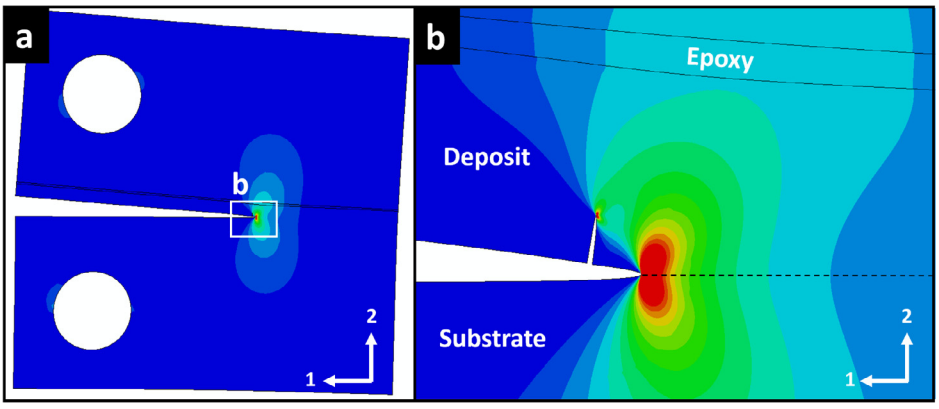

Fig. 11. Interface compact tension K_{Ic} finite element model with opening (S22) stress contours.

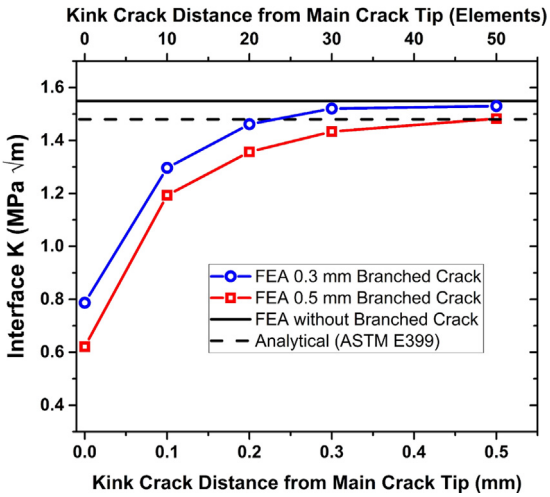

Fig. 12. Effect of branched cracks on the stress intensity of the main crack as a function of distance from the main crack tip.

case the moment is subtracted because it is acting opposite to the applied moment, even though the deformation appears to be in the same direction.

$$G_c = \frac{21(M_{app} - M_{RS})^2}{6\bar{E}IB} \tag{3}$$

Here I is the second moment of area for the composite beam, $\bar{E}$ the plane strain modulus, and the moment due to the residual stress, M_{RS}, is given by

$$M_{RS} = \frac{\bar{E}I}{\rho} \tag{4}$$

Fig. 13 shows the average effective energy release rate broken down into the residual stress contribution, and the critical energy release rate for the sanded and grit blasted conditions. In this geometry, the residual stresses account for approximately 35% of the measured mixed mode energy release rate. The curvature method may appear somewhat crude, but it gives a direct accounting, not of the residual stresses themselves, but of their direct impact on the adhesion toughness of the deposit, which is more useful in this particular case. While knowing the exact magnitude and distribution of the residual stresses would be beneficial for a variety of reasons, this information, even if known, would require a much more complicated model such as a weight function to convert to a stress intensity that can be used with fracture based adhesion measurements. While the optical measurement technique employed here could be improved, since this method skips the difficult to measure residual stresses, and their intervening interpretation to stress intensity, it is likely a fairly accurate estimation of the effect of residual stress on the adhesion toughness.

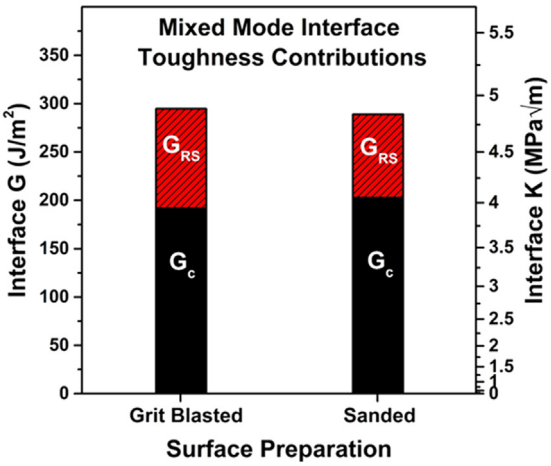

Fig. 13. Interfacial critical energy release rate and energy release rate due to residual stress for the grit blasted and sanded surface preparations.

4.2. Fracture toughness application

Having measured a $K_{I,eff}$ value for this CS system, it is interesting to apply it to the failure observed in the ASTM C633 samples. Because the CS interface is brittle and contains flaws, the failure of the ASTM C633 specimens is much more accurately treated as a classic fracture mechanics problem. Since the adhesion failure stress and the fracture toughness for the grit blasted samples is known, the flaw size required to produce this failure can easily be found using analytical stress intensity solutions. For a circular center crack in an infinite 3d body, the stress intensity solution is given by Eq. (5), where $F = 2/\pi$ [33]. The infinite body assumption is reasonable because the flaw size it gives is < 2% of the diameter of the ASTM C633 specimens, however the center crack geometry leads to lower stress intensity factors than edge cracks. Substituting the average failure stress of the grit blasted samples, known to be 73.5 MPa, and the average $K_{I,eff}$ = 1.25 MPa √m, the crack length required for failure is found to be 227 μm (radius).

$$K = F\sigma\sqrt{\pi a} \tag{5}$$

A more precise solution to this problem is that of an edge crack in a finite cylinder. Solutions for this geometry are in the same form as Eq. (5), but various formulations for crack shape use $2/\pi < F < \sim 0.8$ [34]. This results in minimum edge flaw sizes between 227 μm and 144 μm deep. These flaw sizes are comparable to the size of the grit blasting media (260 μm in diameter) which has been shown to become embedded in the substrate [35]. Because the fracture toughness of the interface is so low the ASTM C633 test may be affected by even small flaws such as embedded grit, machining marks on the side of the specimen or invisible delamination due to residual stresses.

The same basic fracture mechanics calculations can also be used to estimate the true tensile (ASTM C633) bond strength of the CS deposits that exceeded the epoxy strength. If the flaw sizes are assumed to be the same for all three surface preparations (regardless of the actual value) the stress required to fracture the sanded samples for example can be extrapolated from the ratio of the interface fracture toughness, and the known interface failure stress of the grit blasted samples (73.5 MPa), as shown in Eq. (6). This gives estimated tensile interface strengths of 87 MPa and 112 MPa for the sanded and milled conditions, respectively. This type of estimation should be treated cautiously as the interface flaws for each surface preparation may have different sizes or causes.

$$\sigma_{Sand} = \frac{K_{I,Sand}}{K_{I,G.B.}}\sigma_{G.B.} \tag{6}$$

These simple examples show how useful fracture mechanics parameters can be, both for examining fundamental structure-property relationships, and also for potential design applications. The advantages of using fracture toughness to characterize adhesion become even more obvious when it is applied to the design and qualification of repairs, where actual flaw sizes can be measured by inspection.

5. Conclusions

The adhesion strength of cold sprayed AA7075 was measured using two fracture toughness methods along with the commonly used ASTM C633 test. The ASTM C633 test was found to be inadequate because the CS adhesion strength regularly exceeded the strength of the epoxy (~75 MPa). The interfacial CT test, not being limited by the glue strength, found a linear relationship between the adhesion toughness, and the surface roughness of the substrate prior to spraying. The interfacial four-point bend test however showed no difference between the grit blasted and sanded conditions, and found a considerably higher mixed mode adhesion toughness than the interfacial CT test. All three of these tests are affected by residual stresses to varying degrees, however the interfacial four-point bend test gives a convenient method for estimating the effects of residual stresses on the adhesion toughness. The most significant findings are briefly listed below.

1. The interfacial K_I fracture toughness was found to be linearly related to the surface roughness while no such relationship was found in the mixed mode (bending) fracture toughness test.
2. Residual stresses significantly affect the measured adhesion values for all test methods, however the four point bend specimen offers a convenient way of estimating residual stress effects, which were found to account for 35% of the mixed mode adhesion toughness.
3. The interfacial CT test showed the clearest effect of surface preparation, making it the preferred adhesion test method, though the test specimen was found to be susceptible to cracking from residual stresses.

Acknowledgments

This work was performed under the Office of Naval Research grant N00014-15-1-2133 with much appreciation of the help from Mr. W. Nickerson.

Appendix A. Supplementary material

Supplementary data to this article can be found online at https://doi.org/10.1016/j.engfracmech.2018.11.009.

References

[1] Villafuerte J. Modern cold spray: materials process and applications. Ontario: Springer; 2015.
[2] Irissou E, Legoux J, Ryabinin AN, Jodoin B, Moreau C. Review on cold spray process and technology: Part I—Intellectual property. J Therm Spray Tech 2008. https://doi.org/10.1007/s11666-008-9203-3.
[3] Koch GH, Kolijn DT. The heat treatment of the commercial aluminum alloy 7075. J Heat Treat 1979;1(2):3–14.
[4] Naval Safety Center Data Management and Analysis Department, Hobbs E, Eaker K. Commander naval air forces foreign object damage mishap analysis. Retrieved from http://www.public.navy.mil/NAVSAFECEN/Documents/statistics/ops_research/PDF/10-026.pdf.
[5] Samson T, MacDonald D, Fernandez R, Jodoin B. Effect of pulsed waterjet surface preparation on the adhesion strength of cold gas dynamic sprayed aluminum coatings. J Therm Spray Technol 2015;24(6):984–93. https://doi.org/10.1007/s11666-015-0261-z.
[6] Kumar S, Bae G, Lee C. Influence of substrate roughness on bonding mechanism in cold spray. Surf Coat Technol 2016;304:592–605. https://doi.org/10.1016/j.surfcoat.2016.07.082.
[7] Perton M, Costil S, Wong W, Poirier D, Irissou E, Legoux JG, et al. Effect of pulsed laser ablation and continuous laser heating on the adhesion and cohesion of cold sprayed Ti-6Al-4V coatings. J Therm Spray Technol 2012;21(6):1322–33. https://doi.org/10.1007/s11666-012-9812-8.
[8] Rokni MR, Widener CA, Crawford GA, West MK. An investigation into microstructure and mechanical properties of cold sprayed 7075 Al deposition. Mater Sci Eng A 2015;625:19–27. https://doi.org/10.1016/j.msea.2014.11.059.
[9] Younger MS, Eckelmeyer KH. Overcoming residual stresses and machining distortion in the production of aluminum alloy satellite boxes, Sandia Report: SAND2007-6811. 2007.
[10] Rech S, Trentin A, Vezzù S, Vedelago E, Legoux J-G, Irissou E. Different cold spray deposition strategies: single- and multi-layers to repair aluminium alloy components. J Therm Spray Technol 2014;6061:1237–50. https://doi.org/10.1007/s11666-014-0141-y.
[11] Moridi A, Hassani Gangaraj SM, Vezzu S, Guagliano M. Number of passes and thickness effect on mechanical characteristics of cold spray coating. Procedia Eng 2014;74:449–59. https://doi.org/10.1016/j.proeng.2014.06.296.
[12] Xiong Y, Zhuang W, Zhang M. Effect of the thickness of cold sprayed aluminium alloy coating on the adhesive bond strength with an aluminium alloy substrate. Surf Coat Technol 2015;270:259–65. https://doi.org/10.1016/j.surfcoat.2015.02.048.
[13] Cavaliere P, Silvello A. Processing conditions affecting residual stresses and fatigue properties of cold spray deposits. Int J Adv Manuf Technol 2015. https://doi.org/10.1007/s00170-015-7365-y.
[14] Cavaliere P. Cold-spray coatings recent trends and future perspectives. Cham: Springer; 2018.
[15] Yamazaki Y, Arai M, Miyashita Y, Waki H, Suzuki M. Determination of interfacial fracture toughness of thermal spray coatings by indentation. J Therm Spray Technol 2013;22(8):1358–65. https://doi.org/10.1007/s11666-013-9961-4.
[16] Babu MV, Kumarf RK. Fracture mechanics approaches to coating strength evaluation. Eng Fract Mech 1996;55(2):235–48.
[17] Lacombe R. Adhesion measurement methods: theory and practice. Boca Raton: Taylor and Francis; 2006.
[18] Bangstein B, Ellingsen M, Scholl N. A method of fracture toughness measurement and effect of partial annealing on monolithic thick cold sprayed aluminum 6061 deposits, IMECE2016-67178-67178. 2017.
[19] Gavras AG, Lados DA, Champagne VK, Warren RJ. Effects of processing on microstructure evolution and fatigue crack growth mechanisms in cold-spray 6061 aluminum alloy. Int J Fatigue 2018;110:49–62. https://doi.org/10.1016/j.ijfatigue.2018.01.006.
[20] Bakshi SR, Laha T, Balani K, Agarwal A, Karthikeyan J. Effect of carrier gas on mechanical properties and fracture behaviour of cold sprayed aluminium coatings. Surf Eng 2007;23(1):18–22. https://doi.org/10.1179/174329407X161618.
[21] Charalambides PG, Lund J, Evans AG, McMeeking RM. A test specimen for determining the fracture resistance of bimaterial interfaces. J Appl Mech 1989;56(1):77. https://doi.org/10.1115/1.3176069.
[22] Charalambides PG, Cao HC, Lund J, Evans AG. Development of a test method for measuring the mixed mode fracture resistance of bimaterial interfaces. Mech Mater 1990;8:269–83.
[23] Yamazaki Y, Schmidt A, Scholz A. The determination of the delamination resistance in thermal barrier coating system by four-point bending tests. Surf Coat Technol 2006;201(3–4):744–54. https://doi.org/10.1016/j.surfcoat.2005.12.023.
[24] Zhao Y, Shinmi A, Zhao X, Withers PJ, Van Boxel S, Markocsan N, et al. Investigation of interfacial properties of atmospheric plasma sprayed thermal barrier coatings with four-point bending and computed tomography technique. Surf Coat Technol 2012;206(23):4922–9. https://doi.org/10.1016/j.surfcoat.2012.05.099.
[25] Gage D, Kim K, Litteken C, Dauskardt R. Role of friction and loading parameters in four-point bend adhesion measurements. J Mater Res 2008;23(1):87–96. https://doi.org/10.1557/JMR.2008.0001.
[26] Rokni MR, Nardi AT, Champagne VK. Effects of preprocessing on multi-direction properties of aluminum alloy cold-spray deposits. J Therm Spray Technol 2018;27:818–26. https://doi.org/10.1007/s11666-018-0723-1.
[27] White BC, Story WA, Brewer LN, Jordon JB. Fatigue behavior of freestanding AA2024 and AA7075 cold spray deposits. Int J Fatigue 2018;112:355–60. https://doi.org/10.1016/j.ijfatigue.2018.03.007.
[28] Hiese W, Kalthoff JF. Recommendations for the Determination of Valid Mode II Fracture Toughnesses K_{IIc}. West Conshohocken, PA: American Society for Testing and Materials; 1999. p. 74–85.
[29] Banks-Sills L. Application of a mode II fracture specimen to plastically deforming material. Adv Plas 1989;1989:483–6. https://doi.org/10.1016/B978-0-08-040182-9.50119-3.
[30] Banks-Sills L, Sherman D. JII fracture testing of a plastically deforming material. Int J Fract 1991;50(1):15–26. https://doi.org/10.1007/BF00035166.
[31] Theocaris PS. Asymmetric branching of cracks. J Appl Mech 1977;44(4):611–8. https://doi.org/10.1115/1.3424145.
[32] Theocaris PS. Complex stress-intensity factors at bifurcated cracks. J Mech Phys Solids 1971;20:256–79. https://doi.org/10.1016/0022-5096(72)90005-1.
[33] Schijve J. Fatigue of structures and materials. New York: Springer; 2010.
[34] Si E. Stress intensity factors for edge cracks in round bars. Eng Fract Mech 1990;42(6):1035–40. https://doi.org/10.1016/0013-7944(92)90142-2.
[35] Sharma MM, Eden TJ, Golesich BT. Effect of surface preparation on the microstructure, adhesion, and tensile properties of cold-sprayed aluminum coatings on AA2024 substrates. J Therm Spray Technol 2014;24(3):410–22. https://doi.org/10.1007/s11666-014-0175-1.